Journal Pre-proofs

Multi-orbital electronic coupling mediated by integrating multiple-metal hybridizations at ultrafast heating accumulation for efficient electrochemical urea synthesis

Rong Huang, Fang Xue, Peifang Wang, Chongchong Liu, Peilin Huang, Lizhe Liu, Hao Li, Yitingyu Zhou, Gang Zhou

PII: S2095-4956(24)00868-4
DOI: https://doi.org/10.1016/j.jechem.2024.12.016
Reference: JECHEM 4336

To appear in: *Journal of Energy Chemistry*

Received Date: 9 October 2024
Revised Date: 26 November 2024
Accepted Date: 5 December 2024

Please cite this article as: R. Huang, F. Xue, P. Wang, C. Liu, P. Huang, L. Liu, H. Li, Y. Zhou, G. Zhou, Multi-orbital electronic coupling mediated by integrating multiple-metal hybridizations at ultrafast heating accumulation for efficient electrochemical urea synthesis, *Journal of Energy Chemistry* (2024), doi: https://doi.org/10.1016/j.jechem.2024.12.016

Multi-orbital electronic coupling mediated by integrating multiple-metal hybridizations at ultrafast heating accumulation for efficient electrochemical urea synthesis

Rong Huang[a, 1], Fang Xue[b, 1], Peifang Wang[a, *], Chongchong Liu[a], Peilin Huang[a], Lizhe Liu[c, *], Hao Li[a], Yitingyu Zhou[a], Gang Zhou[a, *]

[a] *Key Laboratory of Integrated Regulation and Resource Development on Shallow Lake of Ministry of Education, College of Environment, Hohai University, Nanjing 210098, Jiangsu, China*

[b] *College of Mechanical and Electrical Engineering, Handan University, Handan 056005, Hebei, China*

[c] *Jiangsu Key Laboratory for Nanotechnology and Collaborative Innovation Center of Advanced Microstructures, National Laboratory of Solid State Microstructures, Nanjing University, Nanjing 210093, Jiangsu, China*

[1] *These authors contributed equally to the work.*

* Corresponding authors.

E-mail addresses: pfwang2005@hhu.edu.cn (P. Wang). lzliu@nju.edu.cn (L.Liu). gangzhou@hhu.edu.cn (G. Zhou).

Abstract

Electrocatalytic C–N coupling is an environmentally friendly pathway for reducing CO_2 emissions, nitrate wastewater treatment, and urea production. CeO_2 is a commonly used electrocatalyst for urea synthesis, but its yield was restricted by the deficiency of active sites and the high barrier for C–N coupling. Herein, we employed transient heating to introduce oxygen vacancies as sites for the deposition of single metal atoms, thereby maximizing the atomic utilization as active sites for urea synthesis. The as-prepared CuFe-V-CeO_2 electrocatalyst exhibits the outstanding urea yield rate (3553 mg h^{-1} $g_{cat.}^{-1}$) at −1.5 V versus reversible hydrogen electrode (RHE), surpassing the performance of previously reported electrochemical urea electrocatalysts. Theoretical calculation further revealed the roles of Ce, Cu, and Fe sites in active hydrogen (*H) generation, nitrate treatment, and CO_2 stabilization, respectively. This work offers a novel and effective pathway for the design of electrocatalysts and developing an efficient C–N coupling system for urea production.

Keywords: Electrocatalytic; Urea synthesis; Nitrate treatment; C–N coupling

1. Introduction

Nitrate pollution poses various hazards to the natural environment, such as water eutrophication and algal blooms [1-4]. Moreover, excessive nitrate in drinking water can also cause some serious human diseases, such as tumors, blue baby disease, and liver injury [5,6]. Thus, nitrate pollution is emerging as a serious global concern. The electrocatalytic reduction method has garnered significant attention as an effective approach for nitrate reduction due to its simple process and the use of electrons as a reducing agent, which generates no pollution [7-10]. However, the low value and limited usability of electrocatalytic nitrate reduction products pose significant challenges to their practical application as resources, thereby constraining the broader adoption of this technology for nitrate treatment [11-13]. Therefore, electrocatalytic C–N coupling presents an effective approach for nitrate wastewater treatment. Additionally, the synthesized urea can be utilized as a valuable resource [14]. Currently, commonly used electrocatalytic C–N coupling catalysts primarily include various metal oxides or layered double hydroxides. Among these, CeO_2 has garnered significant attention for its tunable properties and ease of synthesis. The technique of modulating CeO_2 with metal deposition to compensate for its limited active sites and enhance its performance has been widely applied. For example, Wei et al. introduced single-atom Cu as active sites into CeO_2 to accelerate reaction kinetics [15]. Zhan et al. produced a CuAu single-atom alloy on CeO_2 to enhance electronic metal support interaction [16]. Cu and Fe are widely used to modify catalysts due to their ability to optimize active sites and enhance overall catalytic activity. For electrocatalytic urea synthesis, Cu and Fe offer distinct advantages due to their strong adsorption capabilities for $*NO_2$ and $*CO_2$, respectively. These adsorption properties play a

crucial role in facilitating the C–N coupling process, which is a key for efficient urea production. However, traditional methods for depositing Cu and Fe are challenged by issues including poor dispersion of active sites and weak interatomic forces, which hinder catalytic activity and stability in urea electrocatalysis. Thus, a precise atom-anchoring strategy holds great potential for improving catalytic activity and urea yields, addressing critical challenges in sustainable chemical synthesis.

In this work, we prepared a CeO_2 scaffold and introduced vacancies via a Joule heating method to serve as sites for the deposition of single metal atoms (Cu, Fe), thereby maximizing atomic utilization and forming active sites of urea synthesis. The as-prepared CuFe-V-CeO_2 electrocatalyst exhibits an outstanding urea yield rate (3553 mg h^{-1} $g_{cat.}^{-1}$) at −1.5 V versus reversible hydrogen electrode (RHE), superior to that of previously reported electrocatalysts of electrochemical urea synthesis. Electrochemical tests were conducted on the material to confirm its catalytic capability, demonstrating that the material possesses excellent electron transfer ability with minimal reaction barrier. Calculations based on density functional theory (DFT) proved that Ce, Cu, and Fe atoms are respectively excellent sites for hydrogen activation, nitrate treatment, and CO_2 stabilization, promoting C–N coupling and lowering the energy barrier of urea synthesis. This work is dedicated to simultaneously addressing environmental and energy issues, endowing it with great significance.

2. Experimental

2.1. Preparation of CeO_2, CuFe-CeO_2, V-CuFe-CeO_2, and CuFe-V-CeO_2

CeO_2 was synthesized using a hydrothermal method. Typically, 0.85 g of $CeCl_2 \cdot 7H_2O$ was dissolved in 20 mL of deionized water (Solution **A**). 9.6 g of NaOH was dissolved in 15 mL of deionized water (Solution **B**). The Solution **B** was slowly added to Solution **A** under stirring at room temperature. The mixture was then stirred for 30 min before being transferred to a Teflon bottle in the reactor to be hydrothermally treated at 100 °C for 24 h.

The sample was washed alternately with water and ethanol and separated using a centrifuge. This process was repeated three times, after which the samples were dried under vacuum at 60 °C for 12 h. The dried samples were then heated at a ramp rate of 5 °C min^{-1} to 500 °C and annealed for 4 h under an Ar protective atmosphere in a tube furnace to obtain CeO_2.

The powder was then heated in a vacuum environment using a Joule heating device, rapidly reaching approximately 1000 °C (Fig. S1). The optimized parameters for the Joule heating process were a voltage of 15 V and a current of 180 A. The temperature was continuously monitored with a temperature sensor, and dynamic adjustments for the voltage and current were made to maintain stability at 1000 °C

throughout the process. This process introduced oxygen vacancies into CeO_2, thus producing the V-CeO_2 powder. By adjusting the Joule heating temperature, V-CeO_2-800, V-CeO_2-1000, and V-CeO_2-1200 were prepared. Joule heating treatment of CeO_2 at different temperatures results in varying oxygen vacancy concentrations, as shown in Fig. S2.

The doping of Cu and Fe into the material was achieved through a wet chemical impregnation method followed by high-temperature calcination. 50 mg of V-CeO_2 was added to 20 mL of deionized water and stirred for 30 min. Then, 0.84 mL of $CuCl_2 \cdot 2H_2O$ solution (5 mg mL^{-1}) and 0.42 mL of $FeCl_3 \cdot 6H_2O$ solution (5 mg mL^{-1}) were added to the mixture, followed by ultrasonication for 30 min to ensure thorough mixing. Subsequently, 5 mL of Na_2CO_3 solution (50 mg mL^{-1}) was added to the mixture and stirred for 2 h. The product was then separated by centrifugation and freeze-dried. The prepared powder was then heated in an Ar atmosphere containing 5% H_2 at a rate of 5 °C min^{-1} to 250 °C and calcined for 4 h. By adjusting the molar ratio of Cu and Fe, Cu-V-CeO_2, Cu_5Fe_1-V-CeO_2, Cu_3Fe_1-V-CeO_2, Cu_1Fe_1-V-CeO_2, Cu_1Fe_3-V-CeO_2, Cu_1Fe_5-V-CeO_2, and Fe-V-CeO_2 were synthesized.

CuFe-CeO_2 was synthesized by performing wet chemical impregnation and high-temperature calcination on CeO_2 under the same condition. The as-prepared CuFe-CeO_2 powder was then heated in the Joule heating device to approximately 1000 °C to obtain V-CuFe-CeO_2.

2.2. Electrochemical test

Electrochemical experiments were conducted with a three-electrode system on an electrochemical workstation (CIMPS, Zahner, Germany) in an H-cell reactor separated by a cationic membrane (DuPont) (Fig. S3). 5 mg of the as-prepared catalyst was dispersed in the mixed solution composed of 0.6 mL of ethanol, 0.6 mL of water, and 50 μL of 5 wt% Nafion aqueous solution, and then sonicated for 20 min to produce the catalyst ink. After that, 25 μL of the as-prepared ink was dripped onto a 1.0 × 1.0 cm^2 piece of carbon paper to form a working electrode with a mass loading of 0.1 mg cm^{-2}. An Ag/AgCl electrode filled with saturated KCl solution and a platinum sheet were used as the reference electrode and counter electrode, respectively.

The electrolyte utilized for coupling reactions was 0.1 M $KHCO_3$ with 50 mM KNO_3. To ensure CO_2 saturation, CO_2 gas was bubbled through the solution at a flow rate of 30 mL min^{-1} for 30 min prior to the reaction and continuously throughout the reaction. The electrolysis was performed using a chrono-amperometry mode under various steady potentials (−1.2, −1.3, −1.4, −1.5, −1.6, and −1.7 V vs. RHE). The electrochemical process occurred in the cathodic reaction chamber for 1 h under magnetic stirring at the rate of 300 r min^{-1}. The reaction conditions of linear sweep voltammetry (LSV) were the same as those for urea synthesis, with a scan rate of 5

mV s^{-1}. Electrochemical impedance spectroscopy (EIS) spanning a frequency range of 100 kHz to 0.01 Hz was conducted to analyze the resistance of the different catalysts. Double layer capacitance (C_{dl}) was recorded with cyclic voltammetry (CV) method at a non-faradic potential window of 0.65 to 0.75 V vs. RHE. CV curves were measured under different scan rates of 2, 4, 6, 8, and 10 mV s^{-1}.

The potentials measured in the experiment are relative to Ag/AgCl and are converted to reversible hydrogen electrode (RHE) potentials.

$$E_{RHE} = E_{Ag/AgCl} + 0.0591 \times pH + 0.197$$

where the pH values were measured using a pH meter. Specifically, the pH was 8.3 for the electrolyte without CO_2 and 6.1 for the electrolyte with CO_2 introduced.

The C_{dl} was calculated using the following equation.

$$C_{dl} = d(\Delta J)/dv$$

For further information on the quantitative analysis of products generated during the electrocatalytic reaction, please consult Texts S1 and S2.

2.3. Computational method

The study utilized first-principles theory and the Vienna Abinitio Simulation Package (VASP) based on DFT calculations to investigate electronic structures and Gibbs free energy [17]. The calculations employed the generalized gradient approximation (GGA) with the Perdew-Burke-Ernzerhof (PBE) exchange-correlation functional. For the plane-wave basis set, a kinetic energy cutoff of 450 eV was set. Brillouin zone integration was performed using a 3×3×1 Monkhorst-Pack *k*-point grid for both geometry optimization and density of states calculations. The criteria for electron self-consistent iterations and force convergence were set to 10^{-5} eV and 0.02 eV $Å^{-1}$, respectively. A vacuum layer exceeding 15 Å was included in the slab model, with relaxation of intermediates on the surface to prevent surface interactions between periodic slabs. The Gibbs free energy (ΔG) differences for the adsorbed intermediates, including zero-point energy (ZPE), ΔE (electronic energy), and entropy corrections (ΔS), can be described as

$$\Delta G = \Delta E + \Delta E_{ZPE} - T\Delta S$$

With Lobster 4.1.0 software, crystal orbital Hamilton population (COHP) was computed [18]. To search for transition states and obtain the energy barriers, the climbing image nudged elastic band (CINEB) method, employing eight intermediate images, was utilized to determine the transition states and research on the energy barriers [19].

3. Results and discussion

3.1. Structure characterization

As presented in Fig. 1(a), the CeO_2 sample was synthesized via a hydrothermal method. Oxygen vacancies and Cu and Fe sites were introduced separately using Joule heating and wet impregnation followed by calcination, respectively. After synthesis, a range of structural characterizations and theoretical calculations were performed to investigate the material at the micro level. The transmission electron microscopy (TEM) and energy-dispersive spectroscopy (EDS) results were schematically illustrated in Fig. 1(b). The sample consists of nanorods with a diameter of approximately 22 nm, which can also be observed in Fig. S4. Meanwhile, as shown in Fig. S4, compared to the samples with oxygen vacancies introduced via a muffle furnace, those prepared using the Joule heating method exhibit better structural integrity. The elemental mappings in Fig. 1(b) and EDS result in Fig. S5 reveal the uniform distribution of Cu, Fe, Ce, and O in CuFe-V-CeO_2, contributing to the proficient utilization of active sites [20]. In the high-resolution TEM (HRTEM) images of CuFe-V-CeO_2 (Fig. 1c), the lattice spacing of 0.322 nm corresponds to the (111) planes of CeO_2. Under higher resolution, some atomic vacancies (denoted by red line circles) can be found, demonstrating the existence of oxygen vacancies. Along the blue dotted line in Fig. 1(c), the intensity of the peaks shown in Fig. 1(d) is weaker, owning to the presence of oxygen vacancies interrupting the atomic arrangement [21]. Similarly, due to the lower molecular weight of Cu and Fe compared to Ce, their line-scanning intensities are also lower. As shown in Fig. 1(e), the signals on both sides of the oxygen vacancy region are also relatively weak, corresponding to Cu and Fe. This phenomenon aligns with the calculated formation energies depicted in Fig. 1(e). Due to the lower formation energy of Cu and Fe on oxygen vacancies compared to the CeO_2 surface, Cu and Fe atoms tend to be formed on oxygen vacancies. The distance between Cu and Fe formed on oxygen vacancies (3.45 Å) is shorter than that on the CeO_2 surface (3.79 Å), which facilitates the coupling of adsorbed C and N intermediates on the Cu and Fe surfaces.

The crystal phases of the as-synthesized catalysts were characterized by X-ray diffraction (XRD) analysis (Fig. 2a). The diffraction peaks at 28.5°, 33.1°, 47.5°, 56.3°, 59.1°, and 69.4° are indexed to the (1 1 1), (2 0 0), (2 2 0), (3 1 1), (2 2 2), and (4 0 0) facets of CeO_2 phase (PDF#34-0394), respectively [22,23]. These phases can also be observed in the selected area electron diffraction (SAED) shown in Fig. S6. No additional discernible peaks were observed, suggesting that Cu and Fe metals might be atomically dispersed within the catalysts. After Joule heating, the peak intensities increased, indicating the improved crystallinity of the sample. The analysis of oxygen vacancies was conducted using electron paramagnetic resonance (EPR) spectroscopy, with results depicted in Fig. 2(b). Signals corresponding to oxygen vacancies were observed at g = 2.003 for electron-deficient oxygen anions. The intensity of signal exhibits a direct linear correlation with oxygen vacancy concentration [24,25]. After annealing treatment, the signal increased significantly,

indicating a substantial increase in oxygen vacancy concentration. The EPR signal of CuFe-V-CeO_2 is weaker than that of V-CuFe-CeO_2. This is because Cu and Fe are preferentially formed on oxygen vacancies rather than on the CeO_2 surface (Fig. 1e). In the case of CuFe-V-CeO_2, the introduction of metal atoms into the pre-existing oxygen vacancies shields these vacancies, leading to a decrease in signal intensity. Based on the COHP shown in Fig. 2(c), it can be concluded that the existing oxygen vacancies can increase the integral COHP values of Cu and Fe atoms with CeO_2 surface, indicating a stronger atomic bonding.

X-ray photoelectron spectroscopy (XPS) was conducted to analyze the electron transfer between Cu, Fe, and CeO_2. The XPS spectrum of Ce is presented in Fig. 2(d). After introducing oxygen vacancies, Ce gains electrons, causing its characteristic peak to shift toward low binding energy. Upon doping with Cu and Fe, the binding energy of Ce decreases further, indicating the electron transfer from Cu and Fe to Ce. This electron gained reduces Ce oxidation state, thus lowering its binding energy. The XPS results of Cu and Fe are illustrated in Fig. 2(e and f), respectively. After introducing oxygen vacancies, the binding energies of Cu and Fe increase. This is attributed to the introduction of oxygen vacancies resulting in a more stable atomic hybridization between Cu, Fe, and CeO_2, leading to a stronger internal electron transfer. To further determine the chemical valence state of Cu and Fe, the LMM Auger peaks of Cu and Fe in CuFe-V-CeO_2 were measured, as shown in Fig. S7.

3.2. Electrocatalytic urea synthesis

Electrocatalytic urea synthesis was carried out in a cell containing 0.1 M $KHCO_3$ and 50 mM KNO_3. CO_2 gas was introduced into the reactor before and during the reaction. Chronoamperometry (CA) was employed at a fixed potential to measure the reaction. The concentration of urea was quantitatively analyzed through a sodium salicylate method after urease decomposition (Text S1). As shown in Fig. 3(a), the urea yield rate initially increases with rising reaction potential, reaching a peak of 3553 mg h^{-1} $g_{cat.}^{-1}$ at −1.5 V vs. RHE, before eventually declining. This trend occurs because increasing the potential raises the reaction overpotential, thereby accelerating the reaction rate. However, at higher potentials, side reactions such as hydrogen evolution reaction (HER) and nitrate reduction reaction (NO_3RR) are intensified, which ultimately suppresses urea synthesis. As depicted in Fig. 3(b), the Faradaic efficiency (FE) for urea synthesis initially increased with more negative potential before gradually decreasing. CuFe-V-CeO_2 achieved the highest FE of 8.8% at −1.5 V vs. RHE, identified as the optimal potential for urea production. Compared to V-CuFe-CeO_2, which Cu and Fe were doped before vacancy was formed, CuFe-V-CeO_2 exhibits higher urea synthesis efficiency and Faradaic efficiency for urea production. This improvement is attributed to the pre-introduced oxygen vacancies, which facilitate the growth of Cu and Fe on the surface, creating more suitable active sites for C–N coupling. To investigate the roles of oxygen vacancies and bimetallic sites, V-CeO_2 treated at different temperatures and CuFe-V-CeO_2 synthesized with varying metal precursor ratios were prepared as comparison samples. Their urea yield rates

are presented in Fig. S8.

To further elucidate the competition between parallel reactions, we tested the products of NO_3RR, CO_2 reduction reaction (CO_2RR), and HER during urea electrosynthesis process. The total FE distribution of all products at the optimal potential for four catalysts is shown in Fig. 3(c), where NH_3, NO_2^-, and H_2 were identified as the main byproducts. CuFe-V-CeO_2 exhibited a lower yield rate of NO_2^- and NH_3, demonstrating that the urea synthesis reaction on this catalyst surface was more favorable compared to nitrate reduction. To trace the nitrogen source of urea, control experiments were conducted. Urea formation was significant only when both KNO_3 and CO_2 were used as feedstocks simultaneously (Fig. 3d), implying that urea was indeed derived from co-electrolysis. To further verify the nitrogen source of the reaction, nuclear magnetic resonance spectroscopy (NMR) was performed. The ^1H NMR spectrum distinguished $^{14}NH_2CO^{14}NH_2$ and $^{15}NH_2CO^{15}NH_2$ products based on their singlet and doublet chemical signals, respectively. As shown in Fig. 3(e), using $K^{15}NO_3$ as the electrolyte resulted in the ^1H NMR signal splitting into a doublet, confirming that the urea produced originated exclusively from the C–N coupling reaction of CO_2 and KNO_3, rather than from atmospheric N_2. Meanwhile, the ^{13}C isotope labeling experiment was used to confirm that the carbon in urea synthesis originated from the incoming CO_2, as shown in Fig. S9. Moreover, the as-prepared CuFe-V-CeO_2 showed a significantly higher urea yield rate compared with previously reported works (Fig. 3f, Table S1), implying its great prospects in practical urea electrosynthesis. In-situ Fourier transform infrared (FTIR) was also conducted to explain the intermediates in the electrocatalytic synthesis of urea, shown in Fig. S10. *C=O and *C–N vibration bands are located at ~1626 and ~1461 cm^{-1} respectively. The peak intensities reach a maximum at −1.5 V versus RHE, which corresponds to the optimal potential for urea production.

To further investigate the mechanism of electrochemical synthesis of urea, a series of electrochemical tests were conducted. As shown in Fig. 4(a), CuFe-V-CeO_2 exhibited the highest current density in the LSV test, demonstrating its superior electron transfer capabilities for urea synthesis. To assess the electron release capacity of catalysts, EIS test was employed. As shown in Fig. 4(b), the radius of the semicircle in the EIS curve is positively correlated with the surficial resistance (R_{ct}) of the electrode [26]. The radius of Nyquist for CuFe-V-CeO_2 electrode is smaller than that of other electrodes. The smaller charge transfer resistance of the CuFe-V-CeO_2 electrode compared to others indicates that Cu and Fe doping at oxygen vacancies contribute to enhancing electron transfer efficiency. The electrochemical active surface area (ESCA) was assessed using CV method under scan rates ranging from 2 to 10 mV s^{-1} in the non-faradaic region (Fig. S11). Double layer capacitance (C_{dl}) analysis, shown in Fig. 4(c), was employed to estimate the number of active sites on the catalyst. CuFe-V-CeO_2 exhibited the highest C_{dl} value of 8.01 mF cm^{-2} among all synthesized samples. This phenomenon is attributed to the pre-introduced oxygen vacancies, which enhance the utilization efficiency of metal atoms and promote the formation of additional active sites. The ESCA-normalized LSV plot, calculated

based on C_{dl}, is shown in Fig. S12. At the optimal reaction potential (−1.5 V vs. RHE), CuFe-V-CeO_2 still exhibits the highest ESCA-normalized current. Additionally, the CuFe-V-CeO_2 system exhibited the highest effective current density (J = 28.7 mA cm^{-2}, Fig. S13), further demonstrating its superior electron release capability.

The LSV curves under Ar or CO_2 atmospheres, with and without nitrogen sources, are depicted in Fig. 4(d). In the absence of nitrogen sources under an Ar atmosphere, the currents correspond to the HER. Upon the addition of 50 mM KNO_3, distinct signals of nitrate reduction emerge compared to HER. When CO_2 is introduced, the urea synthesis leads to the increased current density and enhanced reaction activity, in agreement with the results in control experiments (Fig. 4d and e). To analyze the variations of the material at different potentials, electrochemical bode tests at various potentials were conducted. As depicted in Fig. 4(e), the most significant decrease in phase angle was observed at potentials around −1.2 to −1.5 V vs. RHE, which closely corresponds to the reaction potential observed in the urea synthesis test (Fig. 3a) and signals the beginning of urea synthesis. The results of cyclic tests are shown in Fig. 4(f). Over ten successive cycles, both the current intensity and urea yield rate remain almost unchanged, demonstrating the superior electrochemical and structural stability of CuFe-V-CeO_2. Meanwhile, the XRD and SEM analyses of the sample before and after the reaction (Fig. S14) indicate that no changes occurred to the catalysis during the reaction process.

3.3. Dynamic analysis

To verify the fundamental mechanism of electrocatalytic urea synthesis, DFT calculations focusing on C–N coupling were carried out. A CuFe-V-CeO_2 model was constructed with Cu and Fe sites placed on a CeO_2 (111) superlattice. The adsorption energies of groups on the material surface are shown in Fig. 5(a). The adsorption energy of $*NO_3$ on Cu sites of CuFe-V-CeO_2 is higher than that on Cu sites of CuFe-CeO_2, and the adsorption energy of $*CO_2$ on Fe sites of CuFe-V-CeO_2 is higher than that on Cu sites of CuFe-CeO_2. This indicates that the Cu and Fe sites on the CuFe-V-CeO_2 surface were more prone to adsorb $*CO_2$ and $*NO_3$, respectively. Meanwhile, active hydrogen (*H) is easier to be generated on Ce sites, which is committed to the hydrogenation reduction of intermediates. Totally, Fe, Cu, and Ce sites played different roles with maximum atomic utilization in the urea electrosynthesis.

The reaction energy profiles for all steps are depicted in Fig. 5(b). CuFe-V-CeO_2 exhibited a low energy demanded to overcome the energy barrier of the rate-determining step (0.76 eV; $*NO_2+*CO_2 \rightarrow *CO_2NO_2$) to realize the first C–N coupling. Achieving rapid and efficient C–N coupling is a prerequisite for the smooth formation of urea and is also the rate-determining step of this reaction. To validate the roles of dual atoms and oxygen vacancies during the reaction, the activation energy of two C–N coupling steps was calculated, with the results shown in Fig. 5(c and d). Compared to single-atom catalysts (Cu-V-CeO_2 and Fe-V-CeO_2) and the catalyst without oxygen

vacancies (CuFe-CeO_2), CuFe-V-CeO_2 exhibited the lowest activation energy in both the first C–N coupling (0.92 eV) and the second C–N coupling (0.25 eV). This highlights the synergistic effect of dual atoms and oxygen vacancies in enhancing catalytic efficiency for C–N coupling reactions. The projected partial density of states (PDOS) of CuFe-V-CeO_2 and CuFe-CeO_2 further disclosed the oxygen vacancy function in urea synthesis. When the oxygen vacancy was doped, the Cu-3*d* orbital has a considerable change when NO_2^- was adsorbed, in which *d* band center (ε_d) was move from −3.41 to −2.07 eV (Fig. 5e). Similarly, the ε_d in Fe site absorbing CO_2 changed from −2.19 to −0.64 eV (Fig. 5f) when oxygen vacancy was introduced. Increased electron occupancy around the Fermi level facilitates electron transfer from Cu to $*CO_2$ and from Fe to $*NO_3$, thus accelerating C–N coupling dynamics.

4. Conclusions

In this work, oxygen vacancies were introduced into CeO_2 via Joule heating to facilitate the targeted growth of Cu and Fe at these sites, resulting in a shorter Cu–Fe distance and a maximized metal atomic utilization. This distinctive structure enriched the active sites and lowered the reaction energy barrier for C–N coupling, significantly improving the reaction selectivity for electrocatalytic urea synthesis. The resulting CuFe-V-CeO_2 electrocatalyst demonstrated an impressive urea yield rate (3553 mg h^{-1} $g_{cat.}^{-1}$) at −1.5 V versus RHE, surpassing most of the reported electrocatalysts. Electrochemical experiments further confirmed its high electron transfer efficiency and excellent stability. DFT calculation revealed that the outstanding catalytic performance can be attributed to the maximized atomic utilization induced by oxygen vacancy and the synergetic contribution of Ce, Cu, and Fe sites. This study provides valuable insights for the design of urea electrosynthesis catalysts and the development of C–N coupling systems.

Declaration of competing interest

The authors declare that they have no known competing financial interests or personal relationships that could have appeared to influence the work reported in this paper.

Acknowledgments

This work was supported by the Hebei Natural Science Foundation (B2024205035). This work was also supported by the Fundamental Research Funds for the Central Universities, and the World-Class Universities (Disciplines), and the Characteristic Development Guidance Funds for the Central Universities (1061-B23017010264). This work was supported by the Fundamental Research Funds for the Natural Science Foundation of China (92047201, 52102237), the Natural Science Foundation of Jiangsu Province (BK20220006), the National Major Projects of Water Pollution Control and Management Technology (2017ZX07204003) and the Postdoctoral Science Foundations of China and Jiangsu Province (2021M690861, 2022T150183, 2021K065A).

Appendix A. Supplementary material

Supplementary data associated with this article can be found, in the online version, at http://dx.doi.org/***.

Reference

[1] R. Biddau, R. Cidu, S. Da Pelo, A. Carletti, G. Ghiglieri, D. Pittalis, Sci. Total Environ. 647 (2019) 1121-1136.

[2] R. Carrey, E. Ballesté, A.R. Blanch, F. Lucena, P. Pons, J.M. López, M. Rull, J. Solà, N. Micola, J. Fraile, T. Garrido, A. Munné, A. Soler, N. Otero, Water Res. 188 (2021) 116537.

[3] G. Vilardi, R. Bubbico, L. Di Palma, N. Verdone, Chem. Eng. Res. Des. 154 (2020) 250-261.

[4] A. Bhatnagar, M. Sillanpää, Chem. Eng. J. 168 (2011) 493-504.

[5] H. Özen, U. Kamber, M. Karaman, S. Gül, E. Atakişi, K. Özcan, O. Atakişi, Exp. Toxicol. Pathol. 66 (2014) 367-375.

[6] H.M.A. Sharif, H.M.F. Khan, S. Ullah, Y. Wang, M. Ahmad, B. Yang, C. Li, M.B . Asif, J. Energy Chem. 95 (2024) 380-406.

[7] S. Popli, U.D. Patel, Sep. Purif. Technol. 179 (2017) 494-503.

[8] J. Ingle, U.D. Patel, J. Water Process Eng. 49 (2022) 103082.

[9] Y.-G. Liu, M. Tian, J. Hou, H.-Y. Jiang, Energy & Fuels 36 (2022) 11323-11358.

[10] S. Yin, R. Cao, Y. Han, J. Shang, J. Zhang, W. Jiang, G. Liu, J. Energy Chem. 96 (2024) 642-668.

[11] L. Lv, Y. Shen, J. Liu, X. Gao, M. Zhou, Y. Zhang, X. Meng, X. Yang, D. Gong, Y. Zheng, Z. Zhou, Appl. Catal. A 645 (2022) 118846.

[12] Y. Qian, J. Lv, X. Liu, Z. Qi, A. Wu, J. Energy Chem. 99 (2024) 50-65

[13] T.H.C. Nguyen, C.H.N. Nguyen, T.H. Le, P. Singh, P. Raizada, S. Mohan, V. Dao, T. Van Nguyen, S.Y. Kim, P. Nguyen-Tri, Q.V. Le, C.C. Nguyen, Sustainable Mater.Technol. 40 (2024) e00917.

[14] C. Wang, W. Gao, W. Hu, W. Wen, S. Wang, X. Zhang, D. Yan, B.Y. Xia, J. Energy Chem. 98 (2024) 294-310.

[15] X. Wei, Y. Liu, X. Zhu, S. Bo, L. Xiao, C. Chen, T.T.T. Nga, Y. He, M. Qiu, C. Xie, D. Wang, Q. Liu, F. Dong, C.-L. Dong, X.-Z. Fu, S. Wang, Adv. Mater. 35 (2023) 2300020.

[16] P. Zhan, J. Zhuang, S. Yang, X. Li, X. Chen, T. Wen, L. Lu, P. Qin, B. Han, Angew. Chem. Int. Ed. (2024). doi: 10.1002/anie.202409019.

[17] J. Hafner, J. Comput. Chem. 29 (2008) 2044-2078.

[18] S. Maintz, V.L. Deringer, A.L. Tchougréeff, R. Dronskowski, J. Comput. Chem. 37 (2016) 1030-1035.

[19] G. Henkelman, B.P. Uberuaga, H. Jónsson, J. Chem. Phys. 113 (2000) 9901-9904.

[20] J.-d. Yi, X. Gao, H. Zhou, W. Chen, Y. Wu, Angew. Chem. Int. Ed. 61 (2022) e202212329..

[21] S. Jin, X. Ma, J. Pan, C. Zhu, S.E. Saji, J. Hu, X. Xu, L. Sun, Z. Yin, Appl. Catal. B 281 (2021) 119477..

[22] B. Liu, C. Li, G. Zhang, X. Yao, S.S.C. Chuang, Z. Li, ACS Catal. 8 (2018) 10446-10456.

[23] C. Song, Q. Zhan, F. Liu, C. Wang, H. Li, X. Wang, X. Guo, Y. Cheng, W. Sun, L. Wang, J. Qian, B. Pan, Angew. Chem. Int. Ed. 61 (2022) e202200406.

[24] R. Schmitt, A. Nenning, O. Kraynis, R. Korobko, A.I. Frenkel, I. Lubomirsky, S. M. Haile, J.L.M. Rupp, Chem. Soc. Rev. 49 (2020) 554-592.

[25] A. Martínez-Arias, J.C. Conesa, J. Soria, Res. Chem. Intermed. 33 (2007) 775-791.

[26] D. Cardenas-Morcoso, R. Ifraemov, M. García-Tecedor, I. Liberman, S. Gimenez, I. Hod, J. Mater. Chem. A 7 (2019) 11143-11149.

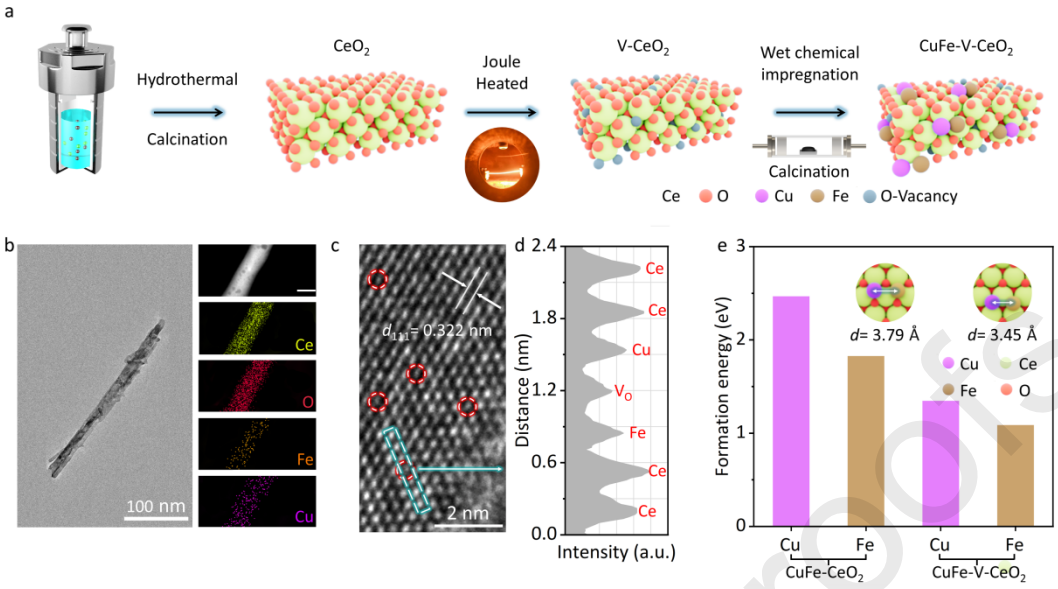

Fig. 1. (a) Diagram for synthetic procedure of CuFe-V-CeO_2. (b) TEM and element mapping of CuFe-V-CeO_2. (c) HRTEM of CuFe-V-CeO_2. (d) Line-scanning intensity profile on oxygen vacancy site in image (c). (e) Formation energy of Cu and Fe on CuFe-V-CeO_2 and CuFe-V-CeO_2.

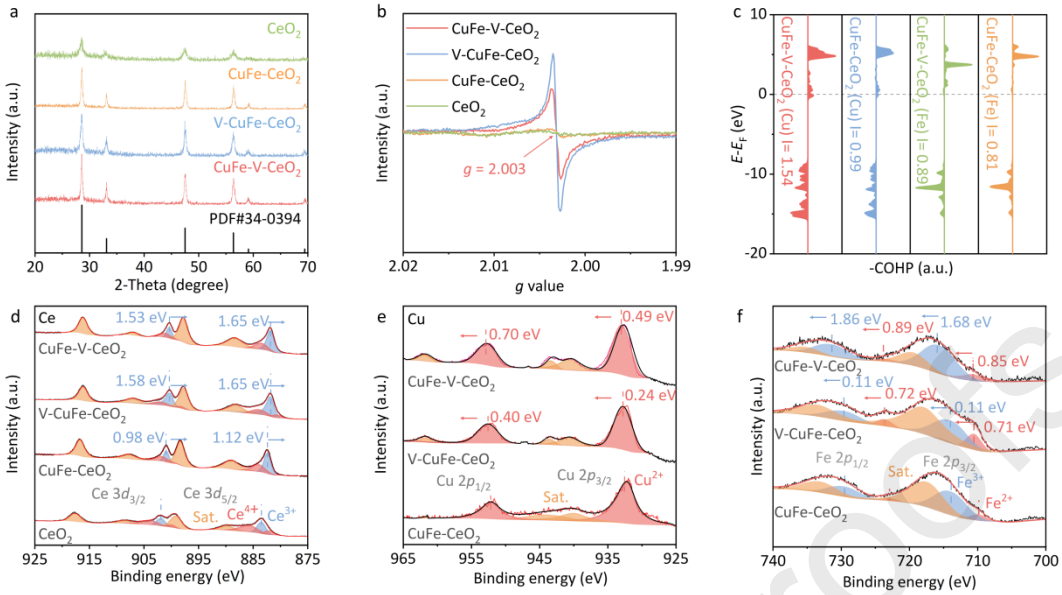

Fig. 2. (a) XRD patterns, (b) EPR patterns, and (c) ICOHP of CeO_2, CuFe-CeO_2, V-CuFe-CeO_2, and CuFe-V-CeO_2. XPS patterns of (d) Ce, (e) Cu, and (f) Fe in different catalysts.

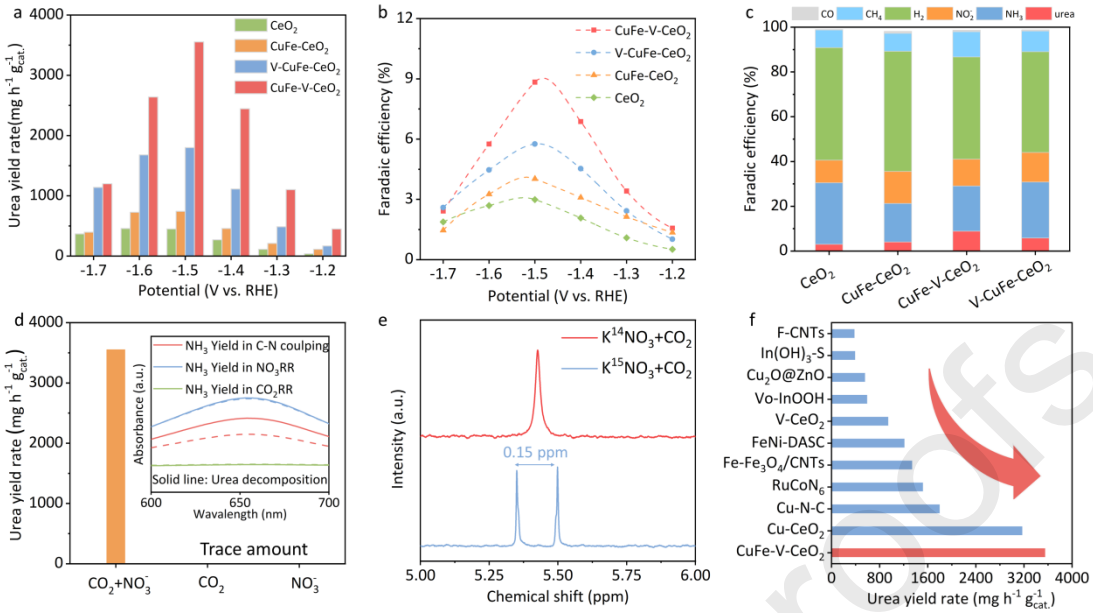

Fig. 3 (a, b) Urea yields and FE of urea for different catalysts at different potentials. (c) FE of different catalysts under their optimal urea production potentials. (d) UV-vis absorption spectra of urea quantification for CuFe-V-CeO_2 with and without C source and N source. (e) ^{1}H NMR spectra obtained by using $K^{14}NO_3$ and $K^{15}NO_3$ as the reactants. (f) Comparison on urea synthesis performance of as-prepared samples with that of reported catalysts with different nitrogen sources.

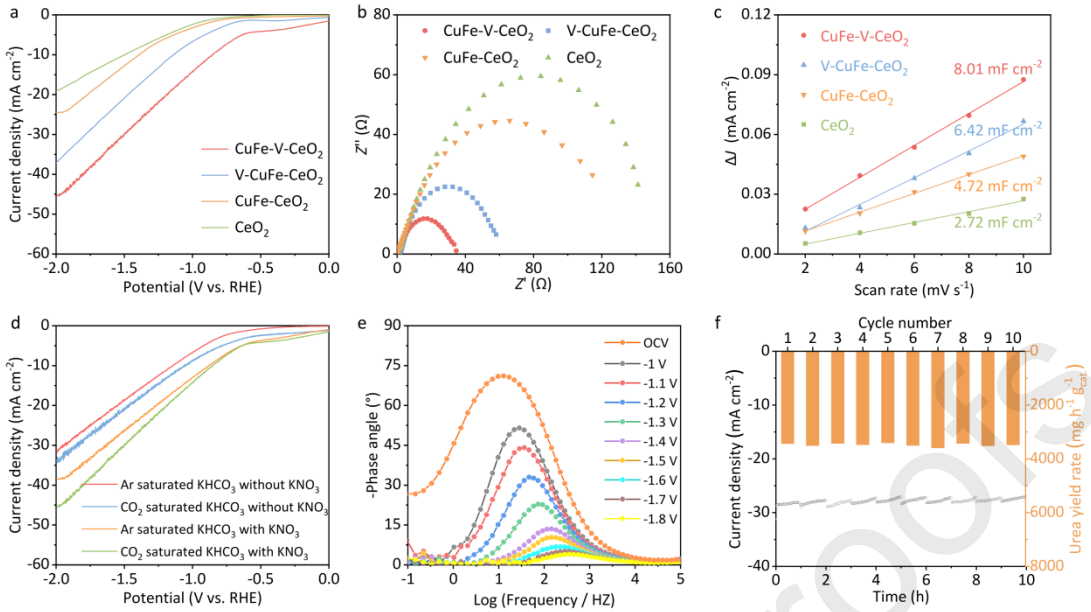

Fig. 4. (a) LSV curves, (b) EIS Nyquist plots, and (c) C_{dl} of different catalysts. (d) LSV curves of CuFe-V-CeO_2 measured in 0.1 M $KHCO_3$ with and without NO_3^--N electrolytes containing Ar or CO_2 flow. (e) Bode plots of CuFe-V-CeO_2 under different potentials. (f) Stability tests of CuFe-V-CeO_2 at −1.5 V versus RHE.

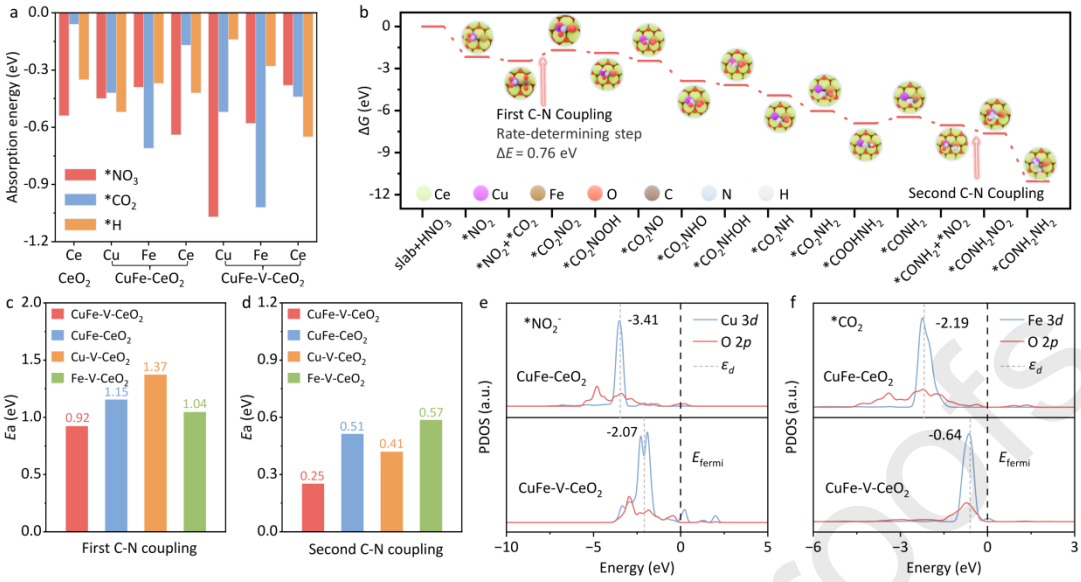

Fig. 5 (a) absorption energy of $*NO_2$, $*CO_2$, and *H on different metal atoms on different catalysts. (b) Free-energy diagram of CuFe-V-CeO_2 for urea production. Activation energy of (c) the first C–N coupling for $*CO_2NO_2$ formation and (d) the second C–N coupling for $*CONO_2NH_2$ formation. PDOS of (e) Cu 3*d* and (f) Fe 3*d* in CuFe-V-CeO_2 and CuFe-CeO_2.

Graphical abstract

By inducing metal atom deposition through oxygen vacancies, CuFe-V-CeO_2 harnesses the synergistic effects of Cu, Fe, and Ce, significantly enhancing electrocatalytic C–N coupling efficiency for urea production.

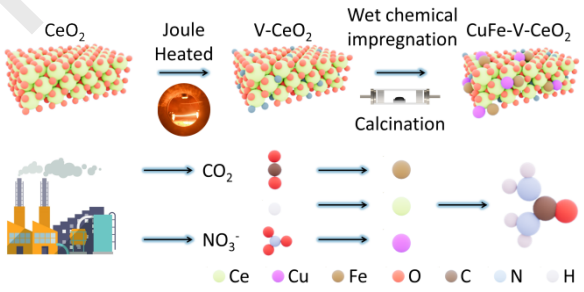

Declaration of interests

☒ The authors declare that they have no known competing financial interests or personal relationships that could have appeared to influence the work reported in this paper.

☐ The author is an Editorial Board Member/Editor-in-Chief/Associate Editor/Guest Editor for *[Journal name]* and was not involved in the editorial review or the decision to publish this article.

☐ The authors declare the following financial interests/personal relationships which may be considered as potential competing interests: